

Full Length Article

Improved cycling performance of $\text{SiO}_x/\text{MgO}/\text{Mg}_2\text{SiO}_4/\text{C}$ composite anode materials for lithium-ion batteryBinbin Xu^a, Honglie Shen^{a,*}, Jiawei Ge^a, Quntao Tang^b^a College of Materials Science & Technology, Jiangsu Key Laboratory of Materials and Technology for Energy Conversion, Nanjing University of Aeronautics & Astronautics, Nanjing 210016, China^b College of Aerospace Engineering, Nanjing University of Aeronautics and Astronautics, Nanjing 210016, China

ARTICLE INFO

ABSTRACT

Keywords:

SiO_x
 MgO
 Hot-water treatment
 Cycling performance
 Rate capability

Silicon suboxide (SiO_x) is considered as one of the potential candidates for next-generation lithium-ion battery (LIB) anode materials. However, the application of this material is limited by volume change during the discharging and charging process and its low initial cycle Coulombic efficiency (ICE). Herein, we report a controllable and cost-effective route to synthesize the $\text{SiO}_x/\text{MgO}/\text{Mg}_2\text{SiO}_4/\text{C}$ (SMC) composite using magnesium-thermic reaction (MTR), hot-water treatment, and carbonization process. Moreover, the composite exhibits a hierarchical buffer structure composed of microspheres. Because of its special dehydration ability to disrupt the hydrolytic cycle, the introduction of MgO is proved to be beneficial to LIBs' cycling performance and rate capability. Besides, with the formation of Mg_2SiO_4 , the consumption of SiO_2 improves the ICE of the SMC anode to 87.48%. The hierarchical microstructure makes the resultant SMC anode exhibit a stable reversible capacity of 550 mAh g^{-1} , which means a high capacity retention ratio of 78.81% after 200 cycles. Furthermore, the specific capacity of SMC anode keeps around 600 mAh g^{-1} at the current density of 800 mA g^{-1} , showing superb rate performance. This work provides a novel approach to taking advantage of by-products of MTR and also demonstrates the potential of industrial application of SiO_x/C anodes.

1. Introduction

The rapid expansion of the portable consumer electronics market and the steady development of electric vehicles facilitate Li-ion battery (LIB) industry's prosperity. In order to break the limit of the low theoretical capacity [1] of commercial carbon-based anode materials and satisfy the increasing demands on better electrochemical performances and stability, more anode materials have been developed. Recently, Silicon suboxide (SiO_x), a substitute for intrinsic silicon materials, has attracted researchers' attention because of its relatively high theoretical capacity (2615 mAh g^{-1}) and much smaller volume expansion during lithiation/delithiation process [2]. The volume expansion can be decreased to around 160% due to the inert SiO_2 phase and the blocking effect of Li_2O and Li silicates forming in the first cycle [3]. Nevertheless, the inert phase's existence results in a low conductivity of SiO_x -based anodes, causing a poor rate capacity. Moreover, the Li_2O and Li silicates make SiO_x perform a lower initial cycle Coulombic efficiency (ICE).

Several strategies have been proposed to deal with these problems of Si-based materials: synthesis of Si/M or SiO_x/M (electrochemically

active or inactive material with Li) composite materials [4,5] or nanostructures with high specific surface area, such as nanowires [6], nanospheres [7], nanotubes [8,9], nanosheets and porous structures [10,11]. As the most common components employed in Si-based composite anodes, carbon can not only provide high conductivity and relative ductility but also form a stable SEI layer during the charge and discharge cycle. Based on these properties, researchers developed various Si/C or SiO_x/C composite with optimized morphology of a high specific surface, providing more active sites for lithium storage and improving the cycling stability and rate performance. For example, Y. Liu et al. synthesized a dual interface SiO_x/C composite with a high reversible specific capacity of 755 mAh g^{-1} after 300 cycles at 100 mA g^{-1} [12]. By designing and preparing a yolk@shell structured SiO_x/C anode with semi-graphitic carbon coating on the exterior and interior surface, Mai's group [13] successfully obtained full cells with a high energy density and stable cycling behavior. Besides, other micro-nanostructures [14], such as silicon @ oxidized mesocarbon microbeads [15] and honeycombed skeletons [16], have been reported. Compared with irregular particles, better dispersibility of spherical

* Corresponding author.

E-mail address: hlsen@nuaa.edu.cn (H. Shen).

composite particles can ensure the full contact between active materials and conductive matrix and evenly distribute stress resulting from the volume expansion, which attracts researchers' attention. For instance, Han et al. reported a CVD process to prepare microspheres with homogeneously dispersed SiO_x and N-doped carbon at the nanoscale [17]. In Guo's work [18], a hierarchical buffer structure composed of watermelon-inspired Si/C microspheres was synthesized to alleviate volume change and particle fracture, dramatically improving the electrochemical performance of Si anode. Some structures like pomegranate and dandelion were also ever designed by many researchers [19–21].

Apart from carbon, researchers have paid more attention to the function of ceramic-based composite materials. Titanium oxide (TiO_2) has been proved to possess a fast lithiation and delithiation rate with minute volume expansion (<4%) and higher operating voltage. The structural stability and integrity could be well improved by introducing a TiO_2 shell to combine with Si-based materials or substitute amorphous carbon shell [22,23]. Similarly, electrochemically stable amorphous Al_2O_3 was mixed and agglomerated with crystalline silicon and Cu_3Si in Kim's work, where the Al_2O_3 phase was demonstrated as the reason for improving cyclability and rate capability [24].

In conventional magnesiothermic reactions (MTR), MgO , the main reaction byproduct, as well as residual Mg and Mg_2Si , were removed by HCl solution [25,26], leaving voids to relieve volume expansion. Recent studies, however, showed that MgO particles could be involved in the fabrication of LIB electrode materials. For example, the hydrophilic property of MgO particles has been investigated. Gnanaraj et al. observed the higher capacity retention of LiMn_2O_4 electrode by modifying MgO [27]. They assumed that the MgO can reduce the detrimental effect of HF from LiPF_6 solutions, but the detailed explanation was not clear. Similar work was also reported by Xiao [28]. Abraham [29] suggested that MgO particles could work as a dehydrating agent to prevent the hydrolysis of LiPF_6 -based electrolytes and keep the stability of LIBs. A similar function of MgO was demonstrated in Kim's work [30], aiming at improving the cycling performance of Lithium-Sulfur Batteries. Recently, Yang et al. successfully synthesized C-SiO-MgSiO₃-Si composites with the help of an in-situ evolution of the MgSiO_3 from MgO and SiO_2 , which showed an outstanding initial Coulombic efficiency without prelithiation [31].

Herein, we report a controllable and cost-effective route to prepare $\text{SiO}_x/\text{MgO}/\text{Mg}_2\text{SiO}_4/\text{C}$ (SMC) composite for LIBs. By adopting a simple 80 °C hot-water post-treatment after the magnesiothermic reaction, electrochemical in-active MgO nanoparticles [28,32] were in-situ prepared and interwoven with SiO_x nanoparticles. After the carbonization process, a hierarchical structure composed of SMC microspheres was prepared. With a evenly distribution of SiO_x , MgO and Mg_2SiO_4 in the spherical structure, the volume change can be controlled homogeneously in all directions, thus suppressing the fracture of anode materials and improving the cycling stability of SMC anode (reversible capacity is retained at 550 mAh g⁻¹ after 200 cycles at 800 mA g⁻¹). The uniformly distributed MgO particles successfully dehydrated the electrolyte and disrupted the generation of HF, preventing susceptible SiO_2 and current collector from corrosion, which improved the rate capability of the SMC anode. Moreover, in the process of forming Mg_2SiO_4 , the consumption of SiO_2 limited the formation of Li silicates at initial cycles, thus endowing a higher ICE for SMC anode.

2. Experiment section

2.1. Preparation of SiO_x and SiO_x/MgO composite

The porous SiO_2 nanoparticles were prepared by a soft template method adopted in our previous work [33]. Porous SiO_2 nanoparticles, Mg powder (100–200 mesh, Sinopharm Chemical reagent Co., LTD, China) and NaCl (99%, Nanjing Chemical Reagent Co., LTD.) were mixed with a mass ratio of 1:1:1. After fully grinding in a mortar, the homogenous mixture was placed in corundum crucible for a six-hour

magesiothermic reaction at 650 °C in a tubular furnace under argon gas ambiance. The reaction product was soaked in hot deionized water (85 °C) for a 12-hour in-situ oxidation process of residual Mg powder. A 10-min centrifugation process then was conducted three times at a rate of 10,000 rpm to remove NaCl sufficiently. Finally, the resultant materials were rinsed twice by ethanol and dried at 80 °C for 12 h in a blast drying oven to obtain the SiO_x/MgO sample. A control group (SiO_x) using a conventional de-magnesium process was prepared with a similar procedure saving a 12-hour-long impurity removal process using 2 M HCl solution (Hydrochloric acid, 37%, Nanjing Chemical Reagent Co., LTD.).

2.2. Carbonization process to prepare SiO_x/C and SMC composites

First of all, 0.5 g SiO_x or SiO_x/MgO was poured into a dispersion solution of CTAB (Hexadecyl trimethyl ammonium Bromide, 99%, Nanjing Chemical Reagent Co., LTD.), $\text{NH}_3\cdot\text{H}_2\text{O}$ (Ammonium Hydroxide, 25%, Aladdin) and distilled water, which was stirred for one hour beforehand. The mixture solution was stirred for one hour again. Hereafter, 0.3 g resorcinol (AR 99.5%, Nanjing Chemical Reagent Co., LTD.) was slowly added into the solution and stirred for one hour. Afterward, 0.4 g formaldehyde solution (38%, Nanjing Chemical Reagent Co., LTD.) was added dropwise and stirred for another hour. The uniform solution was then transferred into a quartz boat, and an ensuing drying process was carried out in a vacuum oven at 90 °C for 12 h. To prepare the SiO_x/C and SMC composites, a three-hour carbonization process was accomplished at 800 °C with a heating rate of 10 °C min⁻¹ in the argon atmosphere. After the carbonization process, SMC composite was washed by 1 M HCl solution to remove exposed MgO and Mg_2SiO_4 on the carbon layer for better conductivity.

2.3. Characterization

Morphology analysis of samples was carried out by FIB-SEM (TESCAN, LYRA3). The morphology and size of nanoscale powdered samples were characterized by TEM (JEOL, JEM-2100F) with EDS mapping (EDS, Oxford). To characterize the crystal structure and phase of the samples, X-Ray diffraction (XRD) patterns were obtained by a diffractometer (Bruker, D8 Advance) using Cu K α radiation at 45 kV and 40 mA from 10° to 80°. The Raman spectra were collected at room temperature with a Raman microscope (Renishaw inVia, 532 nm laser). In addition, X-ray photoelectron spectroscopy (XPS) was achieved with the help of the X-ray photoelectron spectrometer (Thermofisher, Escalab 250XI). The specific surface area and pore distribution were tested by the N_2 absorption-desorption experiment (ASAP 2020).

2.4. Electrochemical measurements

The working electrode consisted of active material ($\text{SiO}_x/\text{MgO}/\text{C}$ or SiO_x/C composite), acetylene black and sodium alginate with a mass ratio of 8:1:1. After dissolving and fully stirring in DI water, the slurry with suitable viscosity was uniformly coated on copper foil, followed by a drying process at 80 °C overnight and 120 °C for 4 h in the vacuum oven. Afterward, the foil coated with the working electrode was cut into a wafer with an area of 1.56 cm², and the mass loading of electrode material was controlled to be around 1.2 mg cm⁻². In this way, the anodes of CR-2032 half-coin cells, using for electrochemical characterization, were prepared. Then, the half-coin cell, mainly composed of the anode, separator (Celgard 2400 polypropylene membrane), and counter electrode (lithium), was assembled in an argon-filled glove box. The electrolyte was made of 1 M LiPF_6 in ethylene carbonate (EC) and dimethyl carbonate (DMC) (1:1 in volume) with 5% FEC. The cycling and rate performance, based on mass-specific capacity, were assessed using the LAND automatic batteries tester (LAND-CT2001a, Wuhan, China). Cycling voltammetry (CV) was performed using an electrochemistry workstation (CHI660D, shanghai, China) in range from 0.01 V

to 3.0 V, whose scan rates were 0.1, 0.3, 0.5, 0.7, 1.0 mV s⁻¹ respectively. Moreover, electrochemical impedance spectroscopy (EIS) was conducted on the same device with the frequency from 0.01 to 10⁶ Hz with a voltage amplitude of 5 mV at room temperature. All the electrochemical measurements were conducted at 25 °C.

3. Results and discussion

In this work, the mid-product, SiO_x/MgO/Mg composite, was prepared by a magnesiothermic process, whose reliability was demonstrated in our previous work [33]. With enough NaCl added into precursors and fully ground, the reaction exotherm can be efficiently regulated, thus keeping the conformity of the reduction degree of SiO₂. Besides, the reduction of SiO₂ makes large amounts of Mg nanoparticles transfer into MgO nanoparticles simultaneously, which can also spread evenly in the mid-product. Afterward, the SiO_x/MgO/Mg composite was treated by two different methods for SiO_x and SiO_x/MgO composite. The HCl treatment process is widely used in obtaining silicon-based material prepared by magnesiothermic reaction, in which residual Mg and its compounds are dissolved in the HCl solution. Nevertheless, it seems to be harmful to the environment and dangerous since the application of acid solution and the vigorous production of hydrogen. Therefore, a method that can evade these drawbacks and transfer residual Mg into MgO is preferable. Inspired by the work reported by Yu [19], we proposed a hot-water treatment process to substitute the HCl treatment process. In order to reduce the impact of particle aggregation, magnetic stirring was applied to assist the hot-treatment process as well as the carbonization process. Furthermore, during the carbonization process, CTAB was added dropwise in distilled water for the precursor solution, making nanoparticles fully disperse in the solution. In this way, the microsphere with evenly distributed SiO_x or Si-Mg-O composite particles wrapped in the carbon layer was prepared. The procedure for fabricating SiO_x/C and SMC composite anode active materials is illustrated in Fig. 1.

Fig. 2 gives the information on morphology, microstructure, and elemental distribution of various composites. As shown in Fig. 2 (a) and

(d), SiO_x/C and SMC composites are both agglomerated as microspheres around 1 μm. Compared with SiO_x/C microspheres, the average size of SMC microspheres is larger. Furthermore, SMC microspheres exhibit a narrower size distribution. It might result from a more hydrophilic composite precursor. With more MgO nanoparticles embedded in the space between SiO_x nanoparticles, the surface of SiO_x/MgO composite aggregates become more hydrophilic, thus increasing their dispersion in precursor solution [34,35]. In addition, CTAB works as a bridge in the precursor solution, where oxide particles and resorcinol are connected to the hydrophilic end and lipophilic end of cationic surfactant. As a result, a more even carbon layer formed on the surface of SMC microspheres than the SiO_x/C microsphere, as shown in the inset TEM images of Fig. 2 (b) and Fig. 2 (e). Furthermore, it's obvious that more voids exist in the interior surface of SMC microspheres (Fig. 2 (b)), which can accommodate the volume change of SiO_x. The porous structures of SMC and SiO_x are examined by Brunauer-Emmett-Teller (BET) tests, whose results are shown in Fig.S4. According to Fig.S4 (a) and (b), the specific surface areas of SMC and SiO_x are 259.152 m² g⁻¹ and 462.424 m² g⁻¹, respectively. These results demonstrate that our prepared SiO_x-based anodes possess a large specific area. Moreover, the smaller specific surface area indicates that the interior structure is denser in the SMC anode, which corresponds to the narrower size distribution shown in the SEM image. However, the mean pore diameter of SMC, 2.965 nm, is larger than that of SiO_x/C, 2.669 nm, as exhibited in Fig.S4 (c) and (d). This phenomenon might be resulted from voids formed in SMC after post HCl treatment. In order to further examine the elemental distribution of the composites, EDS elemental maps of Si, C, Mg, and O elements were obtained. The difference between SiO_x/C composite and SiO_x/MgO/C composite can be shown more directly in the EDS mapping results. The uniform Mg element distribution and the consistency between Mg and O element distribution in Fig. 2 (c) demonstrate that Mg nanoparticles are fully transferred into MgO nanoparticles during the hot-water treatment process. Whereas, the sparse elemental distribution of Mg in Fig. 2 (f) reveals that a large proportion of residual Mg and its compounds are removed by the HCl solution. The microstructures of the prepared

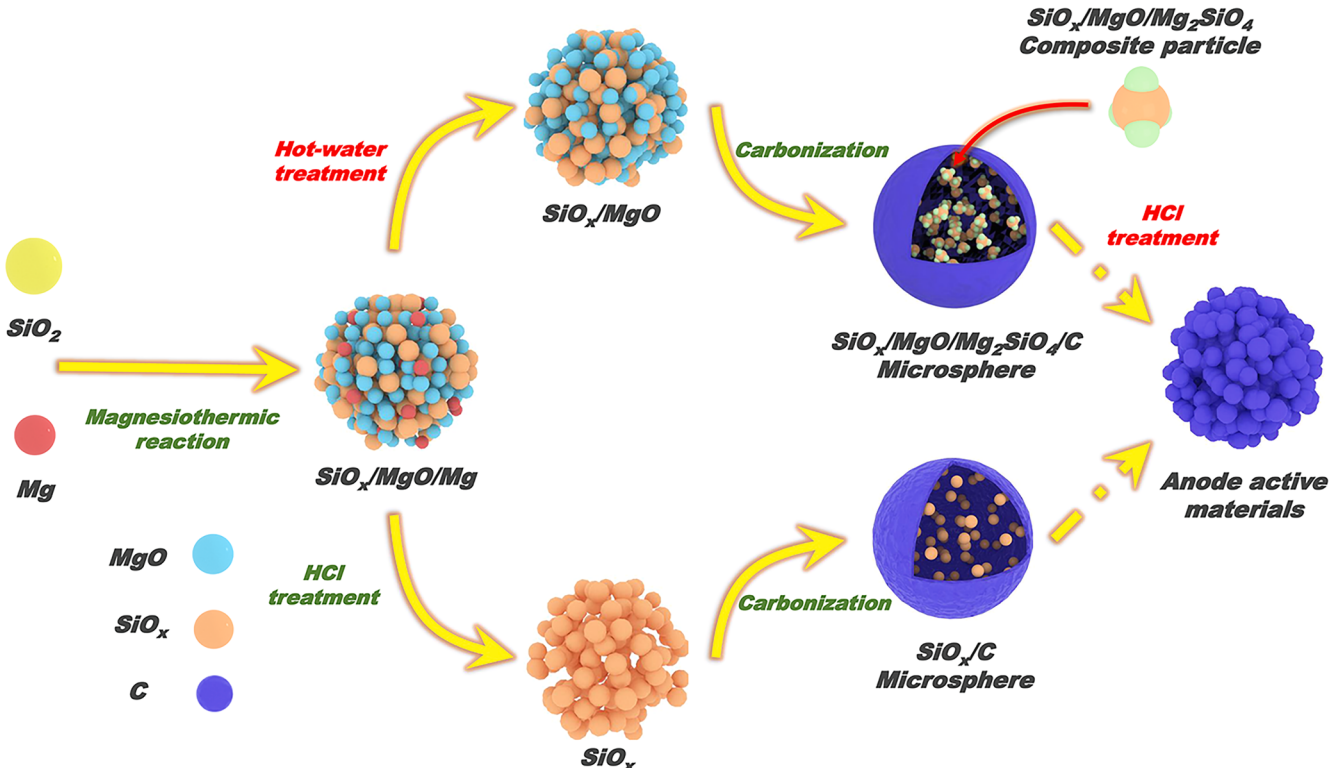


Fig. 1. Schematic illustration of the fabrication process of SiO_x/C and SMC composite anode active materials.

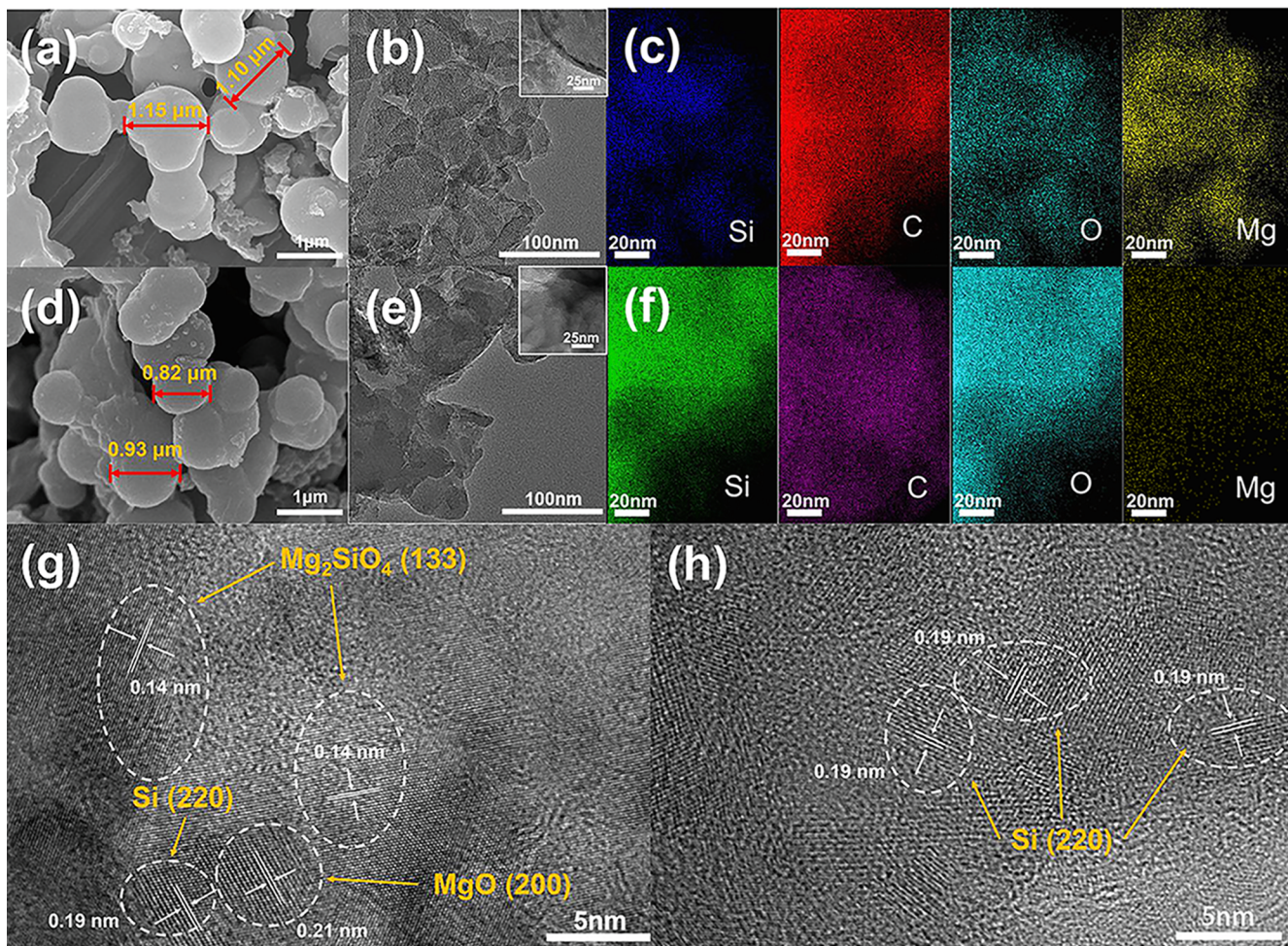
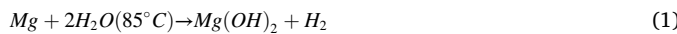


Fig. 2. SEM images of (a) $\text{SiO}_x/\text{MgO}/\text{Mg}_2\text{SiO}_4/\text{C}$ composite and (d) SiO_x/C composite. (b) TEM images and (c) corresponding EDS elemental mapping of $\text{SiO}_x/\text{MgO}/\text{Mg}_2\text{SiO}_4/\text{C}$ composite. (e) TEM images and (f) corresponding EDS elemental mapping of SiO_x/C composite. HRTEM images of (g) $\text{SiO}_x/\text{MgO}/\text{Mg}_2\text{SiO}_4/\text{C}$ composite and (h) SiO_x/C composite.

composite materials were investigated by HRTEM (Fig. 2 (g) and (h)). Fig. 2 (g) confirms the presence of MgO and Mg_2SiO_4 , while the Mg_2SiO_4 phase cannot be observed. It is because the carbonization temperature is only 800°C . At this temperature, the MgO and SiO_2 phase in SiO_x reacts to form Mg_2SiO_4 , while a higher temperature, around 1100°C , is necessary for the formation of the MgSiO_3 . A more detailed mechanism has been reported by Zhang's work [31]. With MgO and Mg_2SiO_4 spreading around SiO_x nanoparticles, the SMC forms a watermelon-like or pomegranate-like structure, as shown in Fig. 1.

XRD analysis was adapted to determine crystal structures in as-fabricated anode materials. As shown in Fig. 3 (a), both samples' XRD patterns exhibit broad SiO_2 peaks and relatively weak crystalline Si diffraction peaks, which indicates the amorphous nature of SiO_x materials. Compared with the sample treated with conventional HCl solution, the MgO and Mg_2SiO_4 diffraction peaks are observed in the patterns of its counterpart treated with hot DI water. The mechanism of the formation of MgO and Mg_2SiO_4 can be illuminated by the following formulas [36,37]:



In high temperatures, the reaction between Mg and H_2O can be

accelerated, and residual Mg nanoparticles are totally transferred into $\text{Mg}(\text{OH})_2$ precipitate in water. However, the temperature of the subsequent dry process is not enough for the chemical transformation from $\text{Mg}(\text{OH})_2$ to MgO . Therefore, the precursor sample for carbonization is a mixture of SiO_x , MgO , and $\text{Mg}(\text{OH})_2$. It is not until the terminal of the carbonization reaction that $\text{Mg}(\text{OH})_2$ decomposes into MgO and H_2O . Meanwhile, MgO reacts with SiO_2 to form Mg_2SiO_4 in 800°C , as demonstrated in Zhang's work [18]. Carbon layers of composite samples are characterized by Raman scattering. From the Raman spectra (Fig. 3 (b)), the two broad peaks, D peak at 1360 cm^{-1} and G peak at 1614 cm^{-1} , are assigned to disordered band and graphite band, respectively. By calculating the ratio of the peak intensity of D peak and G peak (ID/IG), the graphitization degree can be evaluated. The value of ID/IG for SMC is 0.99, which is smaller than that of SiO_x/C , 1.01. It means the graphitization degree of the sample with $\text{MgO}/\text{Mg}_2\text{SiO}_4$ is higher, representing a more uniform and less defective carbon layer, consistent with the morphology observed in Fig. 2 (b) and (e). Besides, the MgO band [38] can also be observed in the Raman spectra of SiO_x/C . There might be a little MgO remaining in the sample after HCl treatment. Furthermore, the broadband around 467 cm^{-1} is the characteristic band of Si-O-Si vibration, implying the successful synthesis of SiO_x for both samples. However, the band of Si-Si vibration, at 517 cm^{-1} , is absent in the spectra for the SiO_x/C sample. We suppose that it might result from the lower degree of crystallization for this sample. Similarly, this phenomenon can be observed in the XPS spectra. To investigate the chemical state of Si and Mg element in various anode materials, Si 2p core-

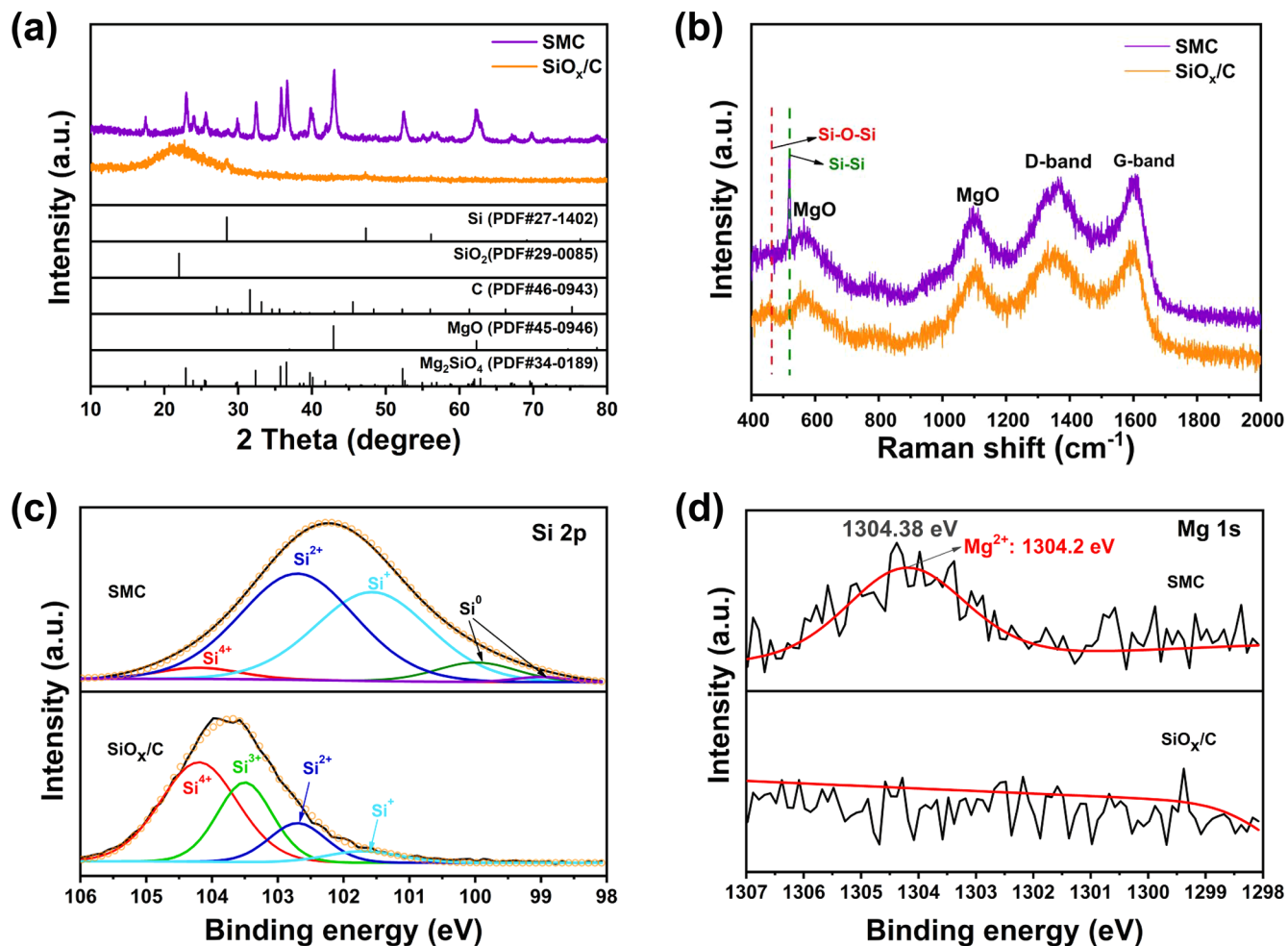


Fig. 3. (a) XRD patterns and (b) Raman spectra of the SMC composite and SiO_x/C composite. XPS spectra of SMC composite and SiO_x/C composite: (c) Si 2p and (d) Mg 1s.

level spectra and Mg 1s core-level spectra were obtained. In Fig. 3 (c), the Si 2p XPS spectrum of SMC is deconvoluted into Si⁴⁺(104.2 eV), Si²⁺(102.7 eV), Si⁺(101.5 eV) and Si (99.8 eV and 98.7 eV). While its counterpart is deconvoluted into Si⁴⁺(104.2 eV), Si³⁺(103.5 eV), Si²⁺(102.7 eV) and Si⁺(101.5 eV) [39–41]. The absence of Si subband implies that almost all SiO_x nanoparticles in SiO_x/C composite exist in an amorphous state. The remarkable difference in Mg 1s spectra (Fig. 3 (d)) [42] indicates that the hot-water treatment and subsequent carbonization successfully transfers residual Mg into MgO and Mg₂SiO₄.

The electrochemical properties of as-prepared Si/C composites were evaluated by assembling them into CR-2032 half-coin cells. Fig. 4 (a) and (b) illustrates the initial three cycles of CV profiles of various anode materials over a potential window from 0.01 V to 3 V at the scan rate of 0.1 mV s⁻¹. The broad peaks between 1.5 and 2.0 V, and the shoulder peak in the range of 0.6–0.9 V in the first cathodic scan can be attributed to the generation of a stable SEI film on the carbon layer [43,44], which disappears during the following cycles. Furthermore, the intense peak in the range of 0.05–0.19 V represents the process of the formation of Li_xSi alloys. In terms of the anodic scan process, the characteristic anodic peaks at around 0.34 V and 0.55 V indicate the complete phase transition from a-LixSi to a-Si. The existence of these redox peaks demonstrates that introducing additional MgO and Mg₂SiO₄ will not affect the intercalation and deintercalation process of lithium ions.

Fig. 4 (c) and (d) display the galvanostatic discharge/charge profiles of SMC and SiO_x/C for the initial three cycles at the current density of 100 mA g⁻¹, respectively. The SMC exhibits a larger reversible capacity (620.1 mAh g⁻¹) as well as higher initial CE (87.49%) than those of

SiO_x/C (507.1 mAh g⁻¹ and 62.12%), which can be ascribed to the higher electron/ion transportation velocity at the interface between carbon layer and oxide nanoparticles. The higher initial capacity benefits from the carbonization process and the decrease of the portion of SiO₂ in SiO_x. With the reaction between MgO and SiO₂, the formation of Mg₂SiO₄ consumes the deleterious SiO₂ phase partially. However, after the initial irreversible capacity loss, the charging and discharging capacity of SiO_x/C tends to be stable, while the relatively large capacity loss still exists between the second and third cycles for SMC. It might result from the electrochemically inactive property of MgO, which retards the generation process of the SEI layer during the initial cycle. Therefore, the irreversible capacity loss in this kind of composite may be a relatively slow process. To further understand the mechanism of the activation process (the initial three cycles), we should pay more attention to the discharging curve of the first cycle. A typical discharging curve of SiO_x/C composite with several potential plateaus at 1.1 V, 0.75 V, and 0.1 V can be observed [33]. The former potential plateau at 1.1 V, corresponding to electrolyte decomposition and the formation of the SEI layer, disappears in the following cycle, demonstrating the stability of the SEI layer formed on the composite surface [45]. Due to a slower SEI layer formation process, the 1.1 V plateau of SMC at the first cycle is not obvious, but it also demonstrates that the electrolysis process is retarded by the hydrophilicity of MgO. With a considerable amount of carbon in these composites, both curves possess an apparent plateau at 0.75 V. Besides, the lower slope of the SMC curve between 0.75 V and 0.1 V, a plateau often regarded as the alloying process of lithium and silicon, indicates that more by-reactions occur on the surface of the composite.

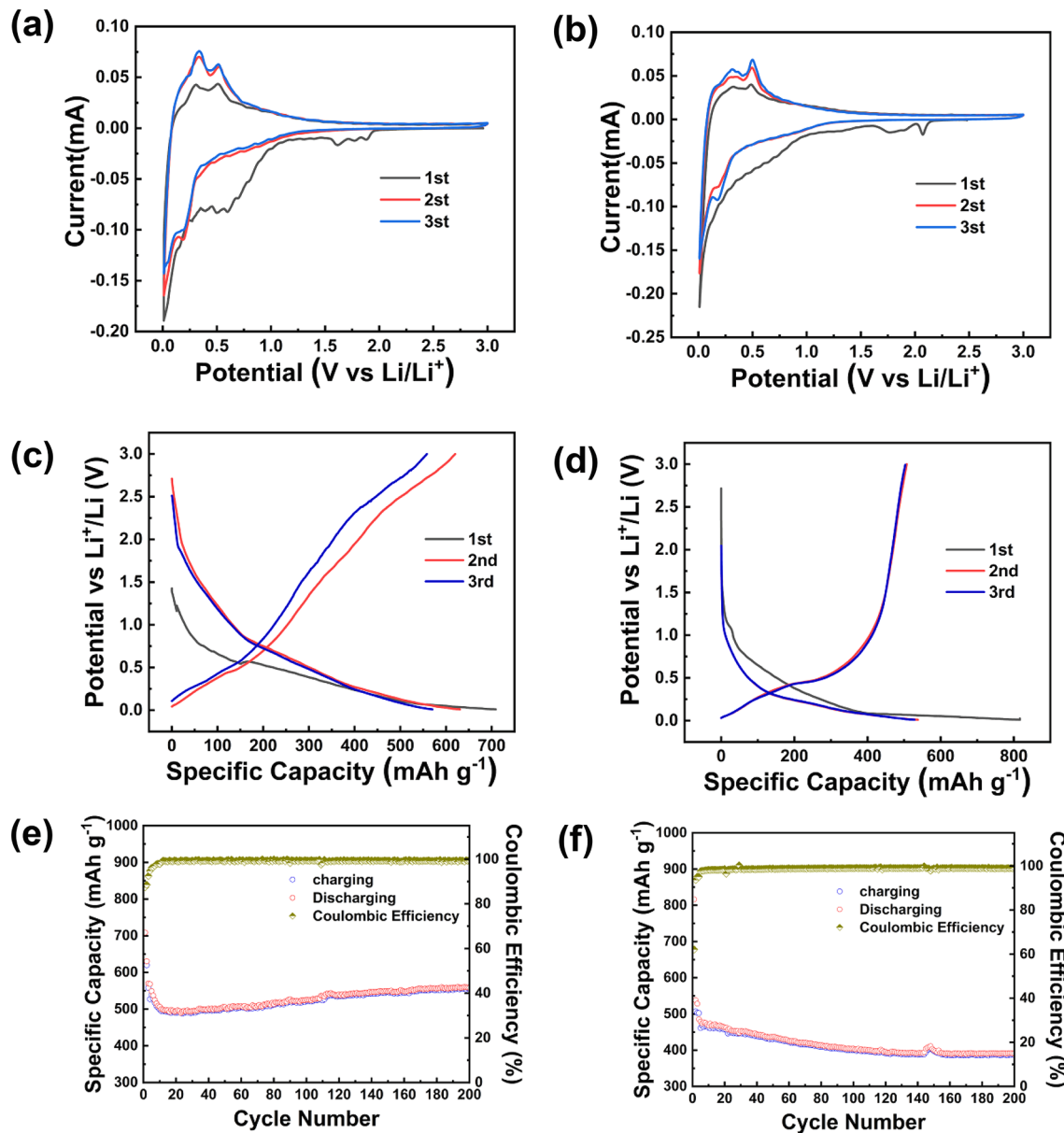


Fig. 4. The electrochemical properties: CV plots of (a) SMC and (b) SiO_x/C at 0.1 mV s⁻¹. First three charge-discharge profiles of (c) SMC and (d) SiO_x/C at 100 mA g⁻¹. Long-term cycling performance of (e) SMC and (f) SiO_x/C at 100 mA g⁻¹ for the first three cycles and then at 800 mA g⁻¹ for 200 cycles.

The long-term cycling stability of SMC and SiO_x/C was evaluated by galvanostatic charging/discharging in the voltage window of 0.01–3 V (vs. Li/Li⁺) at a constant current density of 100 mA g⁻¹ for the initial three cycles and 800 mA g⁻¹ for the following cycles. As shown in Fig. 4 (e), there is a large capacity attenuation at the initial several cycles. The irreversible capacity mainly results from the stable SEI film forming on the uniform carbon layer in SMC anode, and a smaller part can be attributed to the slow formation process of SEI film in the area where SiO_x contacts with the electrolyte. With the presence of Mg₂SiO₄ and voids on the surface in the SMC anode, the volume expansion may not lead to the severe pulverization of the anode. Thus more surface of SiO_x would not be exposed. In this way, the SEI film keeps stable during the following cycles and suppress the large capacity loss. The SMC composite exhibits initial discharge/charge capacities of 708.8/620.1 mAh g⁻¹, indicating the initial Columbic efficiency (ICE) is about 87.48%. Moreover, the average CE is over 98% at the 8th cycle and keeps the high value until the 200th cycle. In contrast, the ICE of SiO_x/C (Fig. 4 (f)) is only 62.10%, whose initial discharge/charge capacity is 507.1/816.5

mAh g⁻¹, but its CE tends to reach a high value (over 95%) within less cycling number. However, the SMC composite anode keeps a higher reversible capacity of 550 mA h g⁻¹ after 200 cycles than its counterpart, around 400 mAh g⁻¹. After 200 cycles, the capacity retention ratio of SMC is 78.81%, while the value of SiO_x/C is only 47.91%. The difference in cycling performance roots in the composition of samples. In other words, it takes more cycles for the sample with more compounds of magnesium to own a more stable SEI layer. The superior cycling stability of LIB made of SMC anode means electrochemically inert MgO and Mg₂SiO₄ nanoparticles can suppress the repeated volume expansion of silicon. Moreover, the SEM images of SiO_x/C and SMC anode foils before and after 200 cycles are given in Fig.S1. Compared with the SiO_x/C anode before cycling (Fig.S1 (a)), obvious cracks appeared after 200 cycles, as shown in Fig. S1(b). While the SMC anode foil kept a good flatness after cycling tests, as exhibited in Fig. S1(d). This phenomenon proves the ability of voids in SMC to mitigate volume expansion. Furthermore, the morphology changes of SMC and SiO_x/C after 200 cycles and their EDS mapping results are shown in Fig.S2 and S3,

respectively. In Fig.S2 (a), the shape of the SiO_x/C microsphere is obviously changed, and there are many flake structures appeared on its surface. This can be attributed to the continual formation of SEI film on the anode. Due to the uneven carbon coating, the stable SEI film could not form on the entire surface of SiO_x/C , and SiO_x would be exposed to the electrolyte, which resulted in a cycle of volume expansion, anode material pulverization, and unstable SEI film formation. As a result, the capacity continued to fade. Nevertheless, the denser hierarchical structure of SMC and uniform carbon layer reduced the harmful contact of SiO_x and the electrolyte, generating a more stable SEI film. For another thing, the larger size of voids forming after post HCl treatment provided more space for volume expansion to avoid the anode pulverization. Moreover, the size of SiO_x/C became smaller. It might be resulted from the corrosion of HF, generating from LiPF_6 hydrolysis. In contrast, as shown in Fig.S3 (a), the SMC microsphere kept its spherical structure and original size, proving that the existence of voids and MgSiO_4 can mitigate the volume expansion and MgO can disrupt the hydrolytic cycle of LiPF_6 .

Apart from the cycling stability, the electrochemical impedance spectra of SiO_x/C and SMC were measured to investigate the effects of active materials on the electrical resistance of anodes. Fig. 5 (a) displays the Nyquist plot of SiO_x/C and SMC, in which all the curves consist of a depressed semicircle in the high-frequency section and a straight line in the low-frequency section. Compared with the curve of SiO_x/C , the depressed semicircle of the SMC curve has a smaller diameter, representing a lower charge-transfer resistance (R_{ct}) at the electrode/electrolyte interface and a lower SEI resistance (R_{sei}). The reduction of contact resistance might result from the good buffering and electronic/ionic conductivity provided by the uniform carbon layer. Furthermore, the electrochemical equivalent circuit for the anodes was fitted by the simulation tool, ZVIEW. As shown in Fig. 5 (a), the equivalent circuit

consists of the solution resistance (R_s), a parallel connection of the SEI resistance (R_{sei}), and corresponding capacitive component (CPE1), in series with the parallel connection of the charge-transfer resistance (R_{ct}) and corresponding capacitive component (CPE2), and a diffusion-related Warburg component (Z_w). The simulation results were shown in Table 1. It is worth noting that the SEI resistance of SiO_x/C is around twice of that of SMC, indicating that a thicker SEI layer forming on the anode [46] and more irreversible consumption of electrolyte. This result also explains the lower ICE of SiO_x/C anode. In addition, smaller charge-transfer resistance indicates more favorable interfacial kinetics in the SMC anode, while the Li^+ ion diffusion kinetics can be analyzed by the Warburg component. According to Eq. (4) [46], Li^+ diffusion coefficient (D_{Li}^+) is proportional to σ^{-2} .

$$D_{\text{Li}^+} = \frac{R^2 T^2}{2A^2 n^4 F^4 C^2 \sigma^2} \quad (4)$$

where R represents the gas constant ($8.314 \text{ J mol}^{-1} \text{ K}^{-1}$); T means absolute temperature; A is the effective electrode surface area; n is the number of electrons per molecule during oxidization; F is the Faraday constant; C represents the Li^+ ion concentration in electrolyte and σ is Warburg coefficient. Commonly, the σ equals the slope of fitting curves in Fig. 5 (b), where the real part of impedance Z' is in direct proportion to $\omega^{-1/2}$. The smaller σ value of SMC exhibits a larger D_{Li}^+ , which might

Table 1
Impedance parameters for SiO_x/C and SMC.

Electrode	R_s/Ω	R_{sei}/Ω	R_{ct}/Ω	$\sigma/\Omega \text{ rad}^{1/2} \text{ s}^{-1/2}$
SMC	2.084	60.76	8.114	174.7
SiO_x/C	2.951	101.1	14.86	800.2

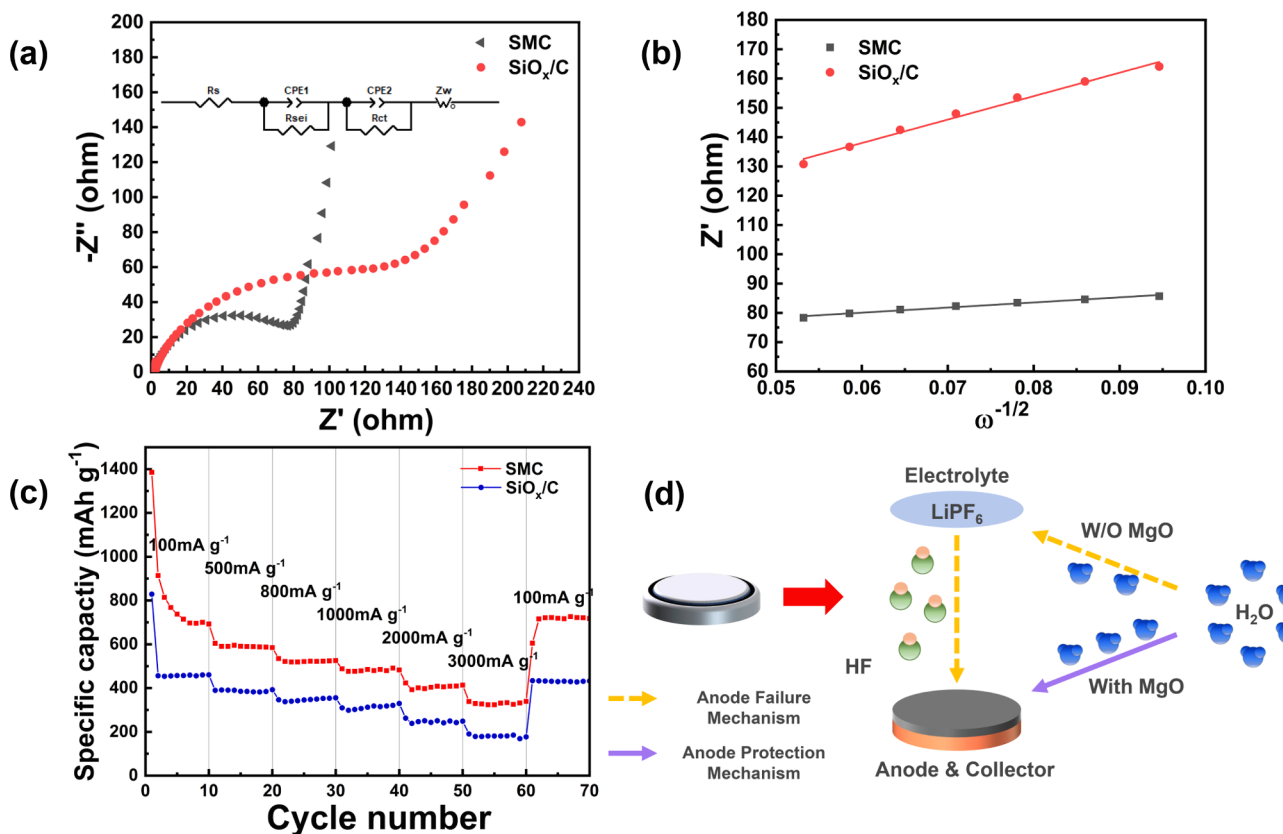


Fig. 5. (a) Nyquist plots of SiO_x/C and SMC. (b) The Plot of real parts of the impedance (Z') versus the reciprocal square root of the angular frequency ($\omega^{-1/2}$). (c) The high-rate capability of the SiO_x/C and SMC composite anode at different current densities from 100 mA g^{-1} to 3000 mA g^{-1} . (d) Diagram illustrating the effect of MgO nanoparticles on cell performance.

benefit from the voids forming during the post HCl treatment after the carbonization process.

The rate performance test was carried out to evaluate the rate capability of anode materials at different current densities from 100 mA g⁻¹ to 3000 mA g⁻¹. As shown in Fig. 5 (c), the specific capacity of SMC keeps around 600 mAh g⁻¹ as the current density is increased to 800 mA g⁻¹. When the current density reaches 2000 mA g⁻¹, its capacity experiences a limited fade. This tendency is similar to that of SiO_x/C anode.

Nevertheless, there is a capacity fade for SiO_x/C anode after the current density returning from 3000 mA g⁻¹ to 100 mA g⁻¹, while SMC anode exhibits the better recovery of capacity. This improvement is attributed to the MgO nanoparticles' ability to interfere with the hydrolytic cycle of LiPF₆, which is referred to in the work reported by Marco-Tulio F. Rodrigues [29]. The hydrolysis reaction can be shown as follows [47]:

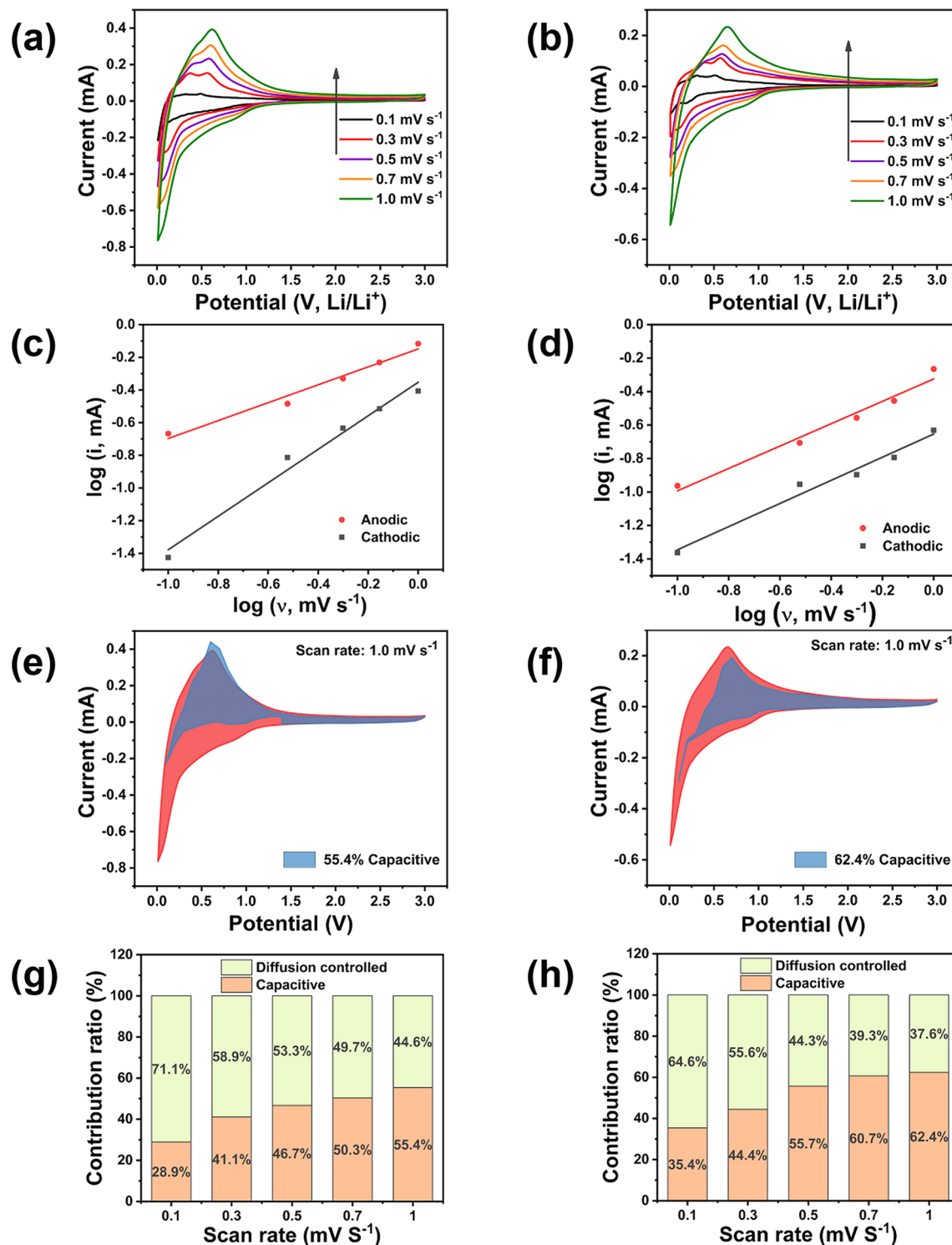
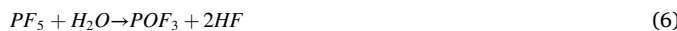


Fig. 6. CV curves at various sweep rates increasing from 0.1 to 1.0 mV⁻¹ for (a) SiO_x/C and (b) SMC. Plots of log (i, peak current) vs. log (v, sweep rate) of the (c) SiO_x/C/Li cell and (d) SMC/Li cell. CV curves with the pseudocapacitive contribution at 1.0 mV s⁻¹ (marking with blue color) for (e) SiO_x/C and (f) SMC. Bar chart of pseudocapacitive contributions at various sweep rates for (g) SiO_x/C and (h) SMC.



As observed in others' work, the dehydration process in oxide ceramics, like MgO, coexists chemical and physical processes. Water is chemisorbed and dissociated on its surface to form thin hydrogel coatings. Then as-formed hydroxylated surface would physisorb extra water, which increases the net moisture uptake. As one of the oxide ceramics, SiO₂ is not suitable for this rule for its solubility to fluoride. The excellent hydrophilic characteristic of MgO distinguishes it from others because of its ability to remove more water from the hydrolytic cycle, which benefits the LIBs. The diagram of the benefit of MgO is illustrated in Fig. 5 (d). With the existence of MgO, the anode material can directly prevent water from participating in the hydrolytic cycle and protects itself and the collector from the corrosion of HF, avoiding failure of the anode.

To investigate the charge storage process of these anode materials, the CV measurements at different scan rates were conducted, as shown in Fig. 6(a) and 6(b). Accordingly, the electrochemical mechanism can be illuminated by fitting the plots of log (i) vs. log (v) at five cathodic/anodic peak pairs. The plot obeys the relationship as follows [48]:

$$\log(i) = a\log(v) + \log(b) \quad (7)$$

Here, a and b are empirical parameters. The electrochemical behaviors could be revealed by the value of a. If the value of a is around 0.5, it indicates that there is diffusion-controlled behavior, whereas the value around 1 means that there is an ideal pseudocapacitive effect. According to Fig. 6(b), the a-value for the SiO_x/C cathodic reaction is 0.94, while that of anodic reaction is 0.59. Similarly, the value of a for the SMC cathodic and anodic reactions are 0.69 and 0.67, respectively. Therefore, the electrochemical process is controlled by diffusion and pseudocapacitive simultaneously. We can evaluate the total pseudocapacitive contribution at a specific scan rate with the help of the following equation:

$$i(V) = k_1 v^{0.5} + k_2 v \quad (8)$$

where $k_1 v^{0.5}$ and $k_2 v$ are the diffusion-controlled insertion process and the pseudocapacitive effect, respectively. As shown in Fig. 6(g) and (h), with the contribution of the large specific surface area of these samples, providing more active sites for the absorption of Li⁺ ion, the pseudocapacitive contributions are both over 50% at high scan rates. Furthermore, with more voids existing in the composite, the diffusion contribution of SMC is smaller, representing a faster diffusion rate, which is consistent with the result of EIS analysis.

4. Conclusions

In summary, the SMC composite anode material for LIBs was prepared by the magnesiothermic reaction, hot-water treatment, and the following carbonization process. In this way, SMC microspheres with uniform phase distribution were successfully prepared and assembled to be a hierarchical buffer structure, exhibiting excellent ability to relieve stress resulting from volume change and hinder the disconnection between the anode material and current collector. Moreover, more voids were generated along with exposed MgO and Mg₂SiO₄ removed by a post-HCl treatment process, which provided more space to accommodate volume expansion. The fabulous structure endows the anode an excellent electrochemical performance. Compared with intrinsic SiO_x/C anode, SMC retained a higher reversible capacity of 550 mAh g⁻¹ after 200 cycles at 800 mA g⁻¹, representing better cycling performance. Moreover, the introduction of MgO, successfully disturbing the electrolytic cycle of LiPF₆-based electrolyte, greatly enhanced the anode's rate capability. The existence of Mg₂SiO₄ also improved the ICE of SiO_x-based anode. Based on the significant improvement of the performance of LIBs and the affordable cost of the treatment, we anticipate that the novel route is feasible for realizing industrial production of SiO_x/C

composite anodes.

CRediT authorship contribution statement

Binbin Xu: Conceptualization, Methodology, Writing - original draft. **Honglie Shen:** Supervision, Project administration, Funding acquisition. **Jiawei Ge:** Software, Formal analysis. **Quntao Tang:** Validation, Resources.

Declaration of Competing Interest

The authors declare that they have no known competing financial interests or personal relationships that could have appeared to influence the work reported in this paper.

Acknowledgment

This work was supported by National Natural Science Foundation of China (617704084); A Project funded by the Priority Academic Program Development of Jiangsu Higher Education Institutions; A Project funded by China Postdoctoral Science Foundation (2019M651823) and the special fund of Jiangsu province for the transformation of scientific and technological achievements (BA2019047).

Appendix A. Supplementary data

Supplementary data to this article can be found online at <https://doi.org/10.1016/j.apsusc.2020.148814>.

References

- [1] Y. Zhang, Y. Zhu, L. Fu, J. Meng, N. Yu, J. Wang, Y. Wu, Si/C composites as negative electrode for high energy lithium ion batteries, Chinese J. Chem. 35 (2017) 21–29.
- [2] J. Hwang, K. Kim, W.S. Jung, H. Choi, J.H. Kim, Facile and scalable synthesis of SiO_x materials for Li-ion negative electrodes, J. Power Sources 436 (2019) 7.
- [3] T. Chen, J. Wu, Q. Zhang, X. Su, Recent advancement of SiO_x based anodes for lithium-ion batteries, J. Power Sources 363 (2017) 126–144.
- [4] Y. Hwa, W.-S. Kim, B.-C. Yu, J.-H. Kim, S.-H. Hong, H.-J. Sohn, Facile synthesis of Si nanoparticles using magnesium silicide reduction and its carbon composite as a high-performance anode for Li ion batteries, J. Power Sources 252 (2014) 144–149.
- [5] S. Chen, C. Ma, Y. Zhu, C. Cao, Interpenetrated tunnel routes in silicon/carbon hollow sphere anodes to boost their lithium storage, Mater. Chem. Front. 4 (2020) 2782–2790.
- [6] W.J. Zhang, Y.Q. Weng, W.C. Shen, R.T. Lv, F.Y. Kang, Z.H. Huang, Scalable synthesis of lotus-seed-pod-like Si/SiO_x@CNF: applications in freestanding electrode and flexible full lithium-ion batteries, Carbon 158 (2020) 163–171.
- [7] X.X. Li, H.B. Shi, L.Q. Zhang, J.B. Chen, P.P. Lu, Novel synthesis of SiO_x/C composite as high-capacity lithium-ion battery anode from silica-carbon binary xerogel, Chin. J. Chem. Eng. 28 (2020) 579–583.
- [8] B. Gattu, R. Epur, P.H. Jampani, R. Kuruba, M.K. Datta, P.N. Kumta, Silicon-carbon core-shell hollow nanotubular configuration high-performance lithium-ion anodes, J. Phys. Chem. C 121 (2017) 9662–9671.
- [9] H. Liu, Y.J. Zou, L.Y. Huang, H. Yin, C.Q. Xi, X. Chen, H.W. Shentu, C. Li, J. Zhang, C.J. Lv, M.Q. Fan, Enhanced electrochemical performance of sandwich-structured polyaniline-wrapped silicon oxide/carbon nanotubes for lithium-ion batteries, Appl. Surf. Sci. 442 (2018) 204–212.
- [10] Z. Wang, N. Yang, L. Ren, X. Wang, X. Zhang, Core-shell structured SiO_x/C with controllable mesopores as anode materials for lithium-ion batteries, Microporous Mesoporous Mater. 307 (2020).
- [11] S.J. Kuang, D.H. Xu, W.Y. Chen, X.Q. Huang, L.Y. Sun, X. Cai, X.Y. Yu, In situ construction of bamboo charcoal derived SiO_x embedded in hierarchical porous carbon framework as stable anode material for superior lithium storage, Appl. Surf. Sci. 521 (2020) 11.
- [12] Y. Liu, J. Ruan, F. Liu, Y. Fan, P. Wang, Synthesis of SiO_x/C composite with dual interface as Li ion battery, J. Alloys Compd. 802 (2019) 704–711.
- [13] Z. Liu, Y. Zhao, R. He, W. Luo, J. Meng, Q. Yu, D. Zhao, L. Zhou, L. Mai, Yolk@Shell SiO_x/C microspheres with semi-graphitic carbon coating on the exterior and interior surfaces for durable lithium storage, Energy Storage Mater. 19 (2019) 299–305.
- [14] N. Lin, T. Xu, T. Li, Y. Han, Y. Qian, Controllable self-assembly of micro-nanostructured Si-embedded graphite/graphene composite anode for high-performance Li-ion batteries, ACS Appl. Mater. Interfaces 9 (2017) 39318–39325.
- [15] H. Liu, Z. Shan, W. Huang, D. Wang, Z. Lin, Z. Cao, P. Chen, S. Meng, L. Chen, Self-assembly of silicon/oxidized mesocarbon microbeads encapsulated in carbon as

- anode material for lithium-ion batteries, *ACS Appl. Mater. Interfaces* 10 (2018) 4715–4725.
- [16] P. Chang, X. Liu, Q. Zhao, Y. Huang, Y. Huang, X. Hu, Constructing three-dimensional honeycombed graphene/silicon skeletons for high-performance Li-ion batteries, *ACS Appl. Mater. Interfaces* 9 (2017) 31879–31886.
- [17] M. Han, Y. Mu, F. Yuan, J. Liang, T. Jiang, X. Bai, J. Yu, Vertical graphene growth on uniformly dispersed sub-nanoscale SiO_x/N-doped carbon composite microspheres with a 3D conductive network and an ultra-low volume deformation for fast and stable lithium-ion storage, *J. Mater. Chem. A*, 8 (2020) 3822.
- [18] X. Quan, L. Jin-Yi, S. Jian-Kun, Y. Ya-Xia, W. Li-Jun, G. Yu-Guo, Watermelon-inspired Si/C microspheres with hierarchical buffer structures for densely compacted lithium-ion battery anodes, *Adv. Energy Mater.* (2016) 1601481.
- [19] N. Liu, Z. Lu, J. Zhao, M.T. McDowell, H.W. Lee, W. Zhao, Y. Cui, A pomegranate-inspired nanoscale design for large-volume-change lithium battery anodes, *Nat. Nanotechnol.* 9 (2014) 187–192.
- [20] J. Lin, J. He, Y. Chen, Q. Li, B. Yu, C. Xu, W. Zhang, Pomegranate-like silicon/nitrogen-doped graphene microspheres as superior-capacity anode for lithium-ion batteries, *Electrochim. Acta* 215 (2016) 667–673.
- [21] X. Luo, H. Zhang, W. Pan, J. Gong, B. Khalid, M. Zhong, H. Wu, SiO_x nanodandelion by laser ablation for anode of lithium-ion battery, *Small* 11 (2015) 6009–6012.
- [22] Y. Jin, S. Li, A. Kushima, X. Zheng, Y. Sun, J. Xie, J. Sun, W. Xue, G. Zhou, J. Wu, F. Shi, R. Zhang, Z. Zhu, K. So, Y. Cui, J. Li, Self-healing SEI enables full-cell cycling of a silicon-majority anode with a coulombic efficiency exceeding 99.9%, *Energy Environ. Sci.* 10 (2017) 580–592.
- [23] W. Luo, Y. Wang, L. Wang, W. Jiang, S.L. Chou, S.X. Dou, H.K. Liu, J. Yang, Silicon/mesoporous carbon/crystalline TiO₂ nanoparticles for highly stable lithium storage, *ACS Nano* 10 (2016) 10524–10532.
- [24] S.-O. Kim, A. Manthiram, Low-cost carbon-coated Si-Cu3Si-Al2O3 nanocomposite anodes for high-performance lithium-ion batteries, *J. Power Sources* 332 (2016) 222–229.
- [25] Z. Bao, M.R. Weatherspoon, S. Shian, Y. Cai, P.D. Graham, S.M. Allan, G. Ahmad, M.B. Dickerson, B.C. Church, Z. Kang, H.W. Abernathy III, C.J. Summers, M. Liu, K. H. Sandhage, Chemical reduction of three-dimensional silica micro-assemblies into microporous silicon replicas, *Nature* 446 (2007) 172–175.
- [26] L.-F. Guo, S.-Y. Zhang, J. Xie, D. Zhen, Y. Jin, K.-Y. Wan, D.-G. Zhuang, W.-Q. Zheng, X.-B. Zhao, Controlled synthesis of nanosized Si by magnesiothermic reduction from diatomite as anode material for Li-ion batteries, *Int. J. Miner. Metall. Mater.* 27 (2020) 515–525.
- [27] J.S. Gnanaraj, V.G. Pol, A. Gedanken, D. Aurbach, Improving the high-temperature performance of LiMn₂O₄ spinel electrodes by coating the active mass with MgO via a sonochemical method, *Electrochim. Commun.* 5 (2003) 940–945.
- [28] B. Xiao, P.-B. Wang, Z.-J. He, Z. Yang, L.-B. Tang, C.-S. An, J.-C. Zheng, Effect of MgO and TiO₂ coating on the electrochemical performance of Li-rich cathode materials for lithium-ion batteries, *Energy Technol.* (2019).
- [29] M.-T.F. Rodrigues, C. Liao, K. Kalaga, I.A. Shkrob, D.P. Abraham, Dehydration rather than HF capture explains performance improvements of Li-ion cells by ceramic nanoparticles, *ACS Appl. Energy Mater.* 2 (2019) 5380–5385.
- [30] R. Ponraj, A.G. Kannan, J.H. Ahn, D.W. Kim, Improvement of cycling performance of lithium-sulfur batteries by using magnesium oxide as a functional additive for trapping lithium polysulfide, *ACS Appl. Mater. Interfaces* 8 (2016) 4000–4006.
- [31] Y. Zhang, G. Guo, C. Chen, Y. Jiao, T. Li, X. Chen, Y. Yang, D. Yang, A. Dong, An affordable manufacturing method to boost the initial Coulombic efficiency of disproportionated SiO lithium-ion battery anodes, *J. Power Sources* 426 (2019) 116–123.
- [32] M. Cai, X. Zhou, Z. Zhao, Q. Ma, H. Xie, X. Li, H. Yin, Engineering electrolytic silicon-carbon composites by tuning the *in situ* magnesium oxide space holder: molten-salt electrolysis of carbon-encapsulated magnesium silicates for preparing lithium-ion battery anodes, *ACS Sustain. Chem. Eng.* 8 (2020) 9866–9874.
- [33] J. Ge, Q. Tang, H. Shen, F. Zhou, H. Zhou, W. Yang, B. Xu, X. Cong, Low-temperature fabrication of porous SiO with carbon shell for high-stability lithium ion battery, *Ceram. Int.* 46 (2020) 12507–12516.
- [34] G. Yang, Q. Guo, D. Yang, P. Peng, J. Li, Disperse ultrafine amorphous SiO₂ nanoparticles synthesized via precipitation and calcination, *Colloids Surf. A* 568 (2019) 445–454.
- [35] S.S. Sainudeen, L.B. Asok, A. Varghese, A.S. Nair, G. Krishnan, Surfactant-driven direct synthesis of a hierarchical hollow MgO nanofiber-nanoparticle composite by electrospinning, *RSC Adv.* 7 (2017) 35160–35168.
- [36] M. Huang, L. Ouyang, Z. Chen, C. Peng, X. Zhu, M. Zhu, Hydrogen production via hydrolysis of Mg-oxide composites, *Int. J. Hydrogen Energy* 42 (2017) 22305–22311.
- [37] T. Shetty, J.A. Szpunar, O. Faye, U. Eduok, A comparative study of hydrogen generation by reaction of ball milled mixture of magnesium powder with two water-soluble salts (NaCl and KCl) in hot water, *Int. J. Hydrogen Energy* 45 (2020) 25890–25899.
- [38] H.S. Kim, H.W. Kim, Fabrication and Raman studies of MgO/SnO₂ core-shell heteronano wires, *Acta Phys. Pol. A* 116 (2009) 58–61.
- [39] Y. Zhang, Z. Mu, J. Lai, Y. Chao, Y. Yang, P. Zhou, Y. Li, W. Yang, Z. Xia, S. Guo, MXene/Si@SiO_x@C layer-by-layer superstructure with autoadjustable function for superior stable lithium storage, *ACS Nano* 13 (2019) 2167–2175.
- [40] K. Kong, G. Xu, Y. Lan, C. Jin, Z. Yue, X. Li, F. Sun, H. Huang, J. Yuan, L. Zhou, Effect of SiO_x-coating crystallinity on electrochemical performance of Si@SiO_x anode materials in lithium-ion batteries, *Appl. Surf. Sci.* 515 (2020).
- [41] J. Hwang, K. Kim, W.-S. Jung, H. Choi, J.-H. Kim, Facile and scalable synthesis of SiO_x materials for Li-ion negative electrodes, *J. Power Sources* 436 (2019).
- [42] C. Feng, Z. Chen, J. Jing, M. Sun, H. Tong, J. Hou, Band structure and enhanced photocatalytic degradation performance of Mg-doped CdS nanorods, *Phys. B Condens. Matter* 594 (2020).
- [43] W. Hong, P. Ge, Y. Jiang, L. Yang, Y. Tian, G. Zou, X. Cao, H. Hou, X. Ji, Yolk-shell-structured bismuth@N-doped carbon anode for lithium-ion battery with high volumetric capacity, *ACS Appl. Mater. Interfaces* 11 (2019) 10829–10840.
- [44] Y.-C. Zhang, Y. You, S. Xin, Y.-X. Yin, J. Zhang, P. Wang, X.-S. Zheng, F.-F. Cao, Y.-G. Guo, Rice husk-derived hierarchical silicon/nitrogen-doped carbon/carbon nanotube spheres as low-cost and high-capacity anodes for lithium-ion batteries, *Nano Energy* 25 (2016) 120–127.
- [45] M.-S. Wang, G.-L. Wang, S. Wang, J. Zhang, J. Wang, W. Zhong, F. Tang, Z.-L. Yang, J. Zheng, X. Li, In situ catalytic growth 3D multi-layers graphene sheets coated nano-silicon anode for high performance lithium-ion batteries, *Chem. Eng. J.* 356 (2019) 895–903.
- [46] X. Chang, B. Sun, Z. Xie, Z. Wang, J. Zheng, X. Li, Structure robustness and Li⁺ diffusion kinetics in amorphous and graphitized carbon based Sn/C composites for lithium-ion batteries, *J. Electroanal. Chem.* 854 (2019).
- [47] M. Stich, M. Göttlinger, M. Kurniawan, U. Schmidt, A. Bund, Hydrolysis of LiPF₆ in carbonate-based electrolytes for lithium-ion batteries and in aqueous media, *J. Phys. Chem. C* 122 (2018) 8836–8842.
- [48] C. Yang, Y. Zhang, J. Zhou, C. Lin, F. Lv, K. Wang, J. Feng, Z. Xu, J. Li, S. Guo, Hollow Si/SiO_xnanosphere/nitrogen-doped carbon superstructure with a double shell and void for high-rate and long-life lithium-ion storage, *J. Mater. Chem. A* 6 (2018) 8039–8046.